Journal of Materials Chemistry A

Increased charge transfer state separation via reduced mixed phase interface in polymer solar cells

Journal:	*Journal of Materials Chemistry A*
Manuscript ID	TA-ART-12-2018-012336.R1
Article Type:	Paper
Date Submitted by the Author:	25-Jan-2019
Complete List of Authors:	Ferron, Thomas; Washington State University College of Arts and Sciences, Physics and Astronomy Waldrip, Matthew; Washington State University College of Arts and Sciences, Physics and Astronomy Pope, Michael; Washington State University College of Arts and Sciences, Physics and Astronomy Collins, Brian; Washington State University College of Arts and Sciences, Physics and Astronomy

Increased charge transfer state separation via reduced mixed phase interface in polymer solar cells

Thomas Ferron, Matthew Waldrip, Michael Pope, Brian A. Collins*
Department of Physics and Astronomy, Washington State University, Pullman, WA 99164

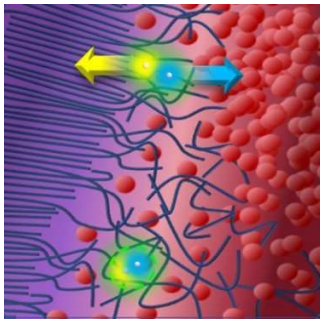

Investigations into bulk heterojunction organic solar cells have demonstrated that molecular mixing within domains and at interfaces significantly impacts device performance. However, these studies often use broad performance metrics that blur fundamental structure-function mechanisms – in particular the role of the mixed phase in charge generation versus charge extraction. Here, we present a new analysis based on time-delayed collection field that separately quantifies each fundamental step in the charge generation process. Additionally, we present a novel resonant X-ray scattering analysis to quantify the state of the three-phase nanostructure (phase volumes and their compositions) as it exists in the devices. We find that in a model semicrystalline system, decreasing the mixed phase interface between pure donor and pure acceptor domains has little effect on the efficiency of charge transfer (CT) state formation but instead dramatically increases the efficiency of CT state separation. While charge extraction efficiencies are affected as well, this has only a minor impact on device performance. With both structure and properties quantitatively resolved for the first time on the exact same devices, we determine a simultaneous >99% (anti)correlation between (mixed)pure phase volume and charge separation efficiency, with values fitting well to an exponential saturation model. This result plus our ability to eliminate other possible contributing factors provides strong evidence of a causal relationship that reducing interfacial mixed phases to establish a steep energy gradient between pure phases aids in charge generation and extraction in organic solar cells.

■ INTRODUCTION

Organic photovoltaics (OPVs) have continued to be an important technology on the frontier of energy research. Solar cells fabricated from polymer or small molecule components bring with them considerable advantages over their inorganic counterparts including the potential for solution printing,[1,2] chemical structures that enable fine tuned properties[3], lead-free and earth-abundant elements, and compatibility for wearable, flexible,[4] and semitransparent technologies.[5] Recent work has seen single junction power conversion efficiencies surpass 14%[6,7] and tandem cells have reached 17.3%.[8] Theoretical models forecast practical efficiencies beyond 20%,[9,10] rivaling common inorganic/hybrid materials. To realize high performance in organic systems, however, massive trial-and-error optimization studies are required over multiple processing parameters for a particular material system, thus slowing progress. Additionally, efforts to design new molecules often lack direction in terms of what moieties will result in what nanostructures. Swiftly approaching efficiency goals will require a more mechanistic and quantitative understanding of fundamental structure-function relationships behind device performance.

The highest efficiency devices are formed from the bulk heterojunction (BHJ) where electron donor and acceptor molecules are cast from a single solvent and phase separated to form an interpenetrating network of domains[11–13]. Morphology investigations have determined that BHJs typically form up to three phases due to a finite donor-acceptor miscibility. Amorphous molecular systems typically form two phases via liquid-liquid phase separation and have been characterized extensively in the past,[14,15] while semicrystalline polymer systems will form three phases: a pure crystalline donor phase, a mixed amorphous phase, and a pure aggregate acceptor phase.[15–18] While pure phases are seen as critical for efficient charge transport,[19–21] the role of the mixed phase is less well understood. Some studies have correlated the presence of a mixed phase with increased photocurrents, suggesting molecular mixing promotes interfacial charge-transfer (CT) states and eventually charge generation.[22–25] Other reports tie increased domain purity to better device fill-factors, suggesting that mixed phases increase charge recombination losses.[15,26] Unfortunately, these metrics (photocurrent and fill factors) depend on many underlying processes, and a more fundamental breakdown of charge generation and recombination dynamics is needed to elucidate the effects of the mixed phase.

Recently, McNeill and coworkers revealed longer charge lifetimes in devices with a higher purity mixed phase and argued that charge extraction must be the main effect on device performance.[27] However, their methods were not able determine whether charge generation or extraction dynamics was the primary influence on device performance. Gorenflot and coworkers have recently made progress on this front via transient absorption spectroscopy

global analysis, although the high excitation fluences used and lack of electrical connections in their samples could impact the measured populations and dynamics.[28] The development of time-delayed collection field (TDCF) by the Neher group, on the other hand, has enabled separate measurement of the charge generation and recombination rates within working devices and at relevant excitation fluences.[29–31] Thus, TDCF could be used to comprehensively quantify device dynamics directly tied to performance in organic solar cells.

Even if such an analysis could be perfected, much uncertainty still lies in quantifying the mixed phase. Previous studies used energy-filtered transmission electron microscopy (EF-TEM) to directly image the presence of the mixed phase and show that it primarily exists at the interface between the two pure phases in blends of poly(3-hexylthiophene) (P3HT) and phenyl-c61-cutyric acid methyl ester PCBM.[16,17,32] Cyclic voltammetry measurements, have revealed cascading energy levels between pure, aggregated phases,[33] indicating that the energy gradient across the interface is highly dependent on the size of the mixed phase. Thus a measurement of phase volumes is useful in probing interfacial width in this system.

Studies have used X-ray or neutron scattering techniques to determine statistical domain purities. In one study, X-ray diffraction intensities were used to quantify phase volumes and compositions.[34] However, in this case diffraction from pure films of the donor molecule were assumed to be 100% crystalline, which may not be accurate, especially for polymers. Neutron scattering has been used to measure mixed phase compositions through measured contrast modulation in the polymer phase.[35] Unfortunately, neutrons cannot distinguish between pure and amorphous polymer phases making phase volume measurements challenging. Most studies that report domain purity quantify total scattering intensity (TSI) of resonant soft X-ray scattering (RSoXS),[27,36–39] but domain purity is convoluted with the number of phases and the respective phase volumes.[14,22,27,40] Because of this, it is unclear in these studies which parameter is actually changing and, therefore, affecting device performance. These studies, furthermore, only assume two phases, which is inappropriate for high-performing semicrystalline polymer systems.[37,41,42] Thus, it would be highly beneficial if a method were developed that could separate and quantify nanophase volumes and compositions in a three-phase system.

In this study we report both a method to separately quantify the phase volumes and compositions within a three-phase, semicrystalline organic blend as well as measure the quantum efficiency of each of the fundamental excited state transitions in the charge generation process of an organic solar cell. Improving on previous scattering models,[43,44] we combine an analysis of RSoXS and X-ray diffraction to quantify the state of the three phase BHJ morphology – in particular the mixed phase. We additionally fully characterize device dynamics and their impact on the device performance by combining optical spectroscopies and TDCF. These analyses are applied to a model semicrystalline polymer:fullerene blend P3HT:PCBM where the phase volume fractions are varied via the fullerene concentration. By conducting structure, dynamics, and performance measurements on the exact same devices, we reveal definitive correlations of CT state separation and free charge recombination dynamics with the pure and mixed phase volumes and critically which is most important for device performance. We find that a reduction in the mixed phase volume across the donor/acceptor interface dramatically improves the charge separation efficiency and is the main driver of device efficiency. While charge extraction efficiency improves as well, this is not enough to significantly suppress charge recombination losses. These results further support the growing theory that a steep energy gradient across the interface between pure domains assist in splitting CT states and improve device performance. [33,45–47]

■ RESULTS & DISCUSSION

Photovoltaic Performance. Overall device performance is summarized in Figure 1 and reveal all PCBM concentrations form a photovoltaic device, even those containing only 5 wt. % PCBM. Critical parameters are extracted and presented Figure 1b and c as a function of increasing PCBM wt.%. The most prominent change in device performance comes from the short circuit current increasing from 0.13 to 10.1 mA/cm^2 with most of the improvement occurring between 20-40 wt.% PCBM. V_{oc} sees its largest change earlier (between 5-10 wt. % PCBM), followed by a modest growth to a maximum of $0.64V$. FF sees its biggest increase between 30-40 wt.% PCBM before plateauing around 52% for the highest performing devices. The optimum concentration of PCBM is in agreement with previous studies.[48,49]

To better understand driving forces behind the device performance trends we turn to quantify the charge generation process. This involves four fundamental steps with an associated efficiency η: photon absorption into the device active layer forming a Frenkel exciton η_{Abs}, exciton diffusion to a donor/acceptor interface to create a CT state η_{CT}, potentially voltage-dependent CT state separation into free charges $\eta_{sep}(V)$, and lastly voltage-dependent charge extraction at the electrodes $\eta_{ext}(V)$. Corresponding losses in the last two steps are termed geminate and bimolecular

recombination, respectively. In our work, these efficiencies are defined such that they multiply together with the incident irradiance to determine the voltage-dependent photocurrent of the device under 1-sun illumination.

Photo-absorption and CT state formation. First, we calculate η_{abs} via transmission UV-Vis absorption measurements shown in Figure 2a. Spectrally, all films show P3HT with distinct 0-0 and 0-1 optical transitions indicating good polymer aggregation.[50] As expected, increasing the total wt.% of PCBM both decreases P3HT peak intensity and correspondingly increases the contribution of PCBM below 400 nm. We use the transfer matrix method to calculate the efficiency of photon absorption within the full device (Figure S2).[51] Although our measurements reveal an overall decrease in optical density upon increasing PCBM wt.% we find, due to the optically thick films used, the absorption efficiency remains fairly constant across all devices. Only slight variations are apparent in the photo-absorption of the active layer at wavelengths $< 400nm$ while the rest of the spectra remains above 80%.

We next use photoluminescence quenching (PLQ) as a measure of radiative recombination of excitons who fail to diffuse to a donor/acceptor interface,[22,52,53] thus revealing η_{CT}. Thickness normalized PL spectra are given in Figure 2b along with reference spectra for pure P3HT and PCBM. Each device is found to exhibit high levels of quenching with qualitatively similar vibronic structure. A noticeable shoulder centered around $910nm$ develops with increasing PCBM wt.% that we attribute to PL from PCBM aggregates as seen in the pure reference sample. While fullerene PL is historically ignored as a factor in quenching efficiency[54] we find that it contributes a measurable signal within our devices and is a sign of a PCBM pure aggregate phase that exists in the blend film that is at least on the length scale of the exciton diffusion length. PLQ is calculated by comparing the integrated blend signal to that of the pure spectra (see supporting information for details) and is found to be approximately 90-92% with only one sample (5 wt.%) at 84% quenched. Thus, each sample has a similar chance for excitons to reach an interface with PCBM distributing the active layer even at low concentrations. Combining this information with our absorption efficiency we can say that in all devices, $70-77\%$ of incident photons convert into CT states. Looking back at the dramatic increase in device performance, we can conclude that neither photon harvesting nor the number of CT states formed are responsible for the performance trends in these devices. Charge loss must then come from mechanisms following the formation of CT states in the form of either geminate or biomolecular recombination.

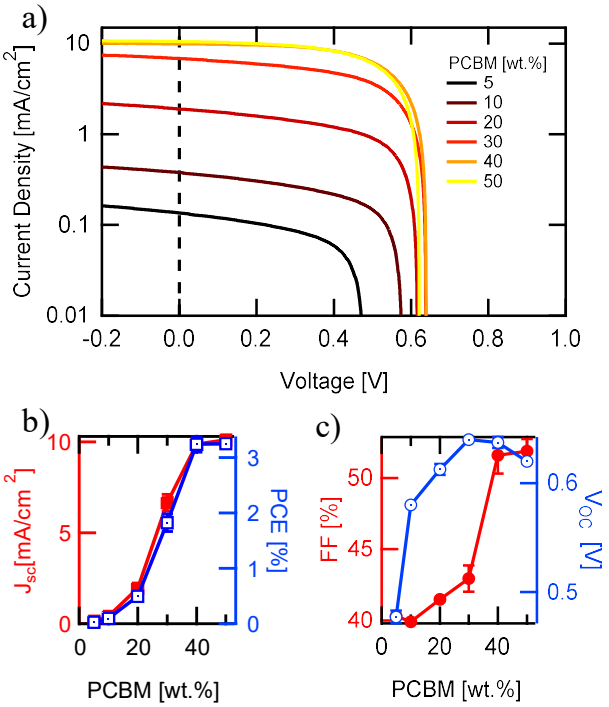

Figure 1: (a) J-V curves for all fabricated devices. Log scaling is used to more readily allow visual inspection of low performing devices. (b) Short circuit current (J_{SC}) and power conversion efficiency (PCE) as a function of PCBM wt.%. (c) Fill factor (FF) and open circuit voltage (V_{oc}) as a function of PCBM wt.%. Tabulated list in the supporting information.

Charge separation and extraction. Measurement of the last two steps in the charge generation process (charge separation and extraction) critically depend on TDCF experiments. TDCF is an optical pump, electronic probe experiment. First, a nanosecond laser pulse excites charges within a device while it is held at an operating bias (V_{pre}). After a delay (t_d), free charges are swept out of the device via an electronic extraction pulse, which quickly switches the device to a collection bias ($V_{coll} = -5V$). The lifetime of the CT state ($\sim 1\ ns$) and the lifetime of free charges Figure S6) provide a window of time that the electronic probe pulse has to sweep out the generated charges before bimolecular recombination takes place. Thus, by setting $t_d = 10\ ns$, we can directly measure the generation current (Figure S4). Conversely, by increasing t_d we can probe the lifetime of free charges and measure losses due to bimolecular recombination effects.

Figure 2c gives the photocurrent of each device plotted along with the generation current density (J_{gen}) as a function of operating bias (V_{pre}), which allows us to investigate how the internal electric field affects the rate of charge generation. In all devices investigated charge separation is independent of applied electric field. This result is consistent with previous P3HT:PCBM TDCF

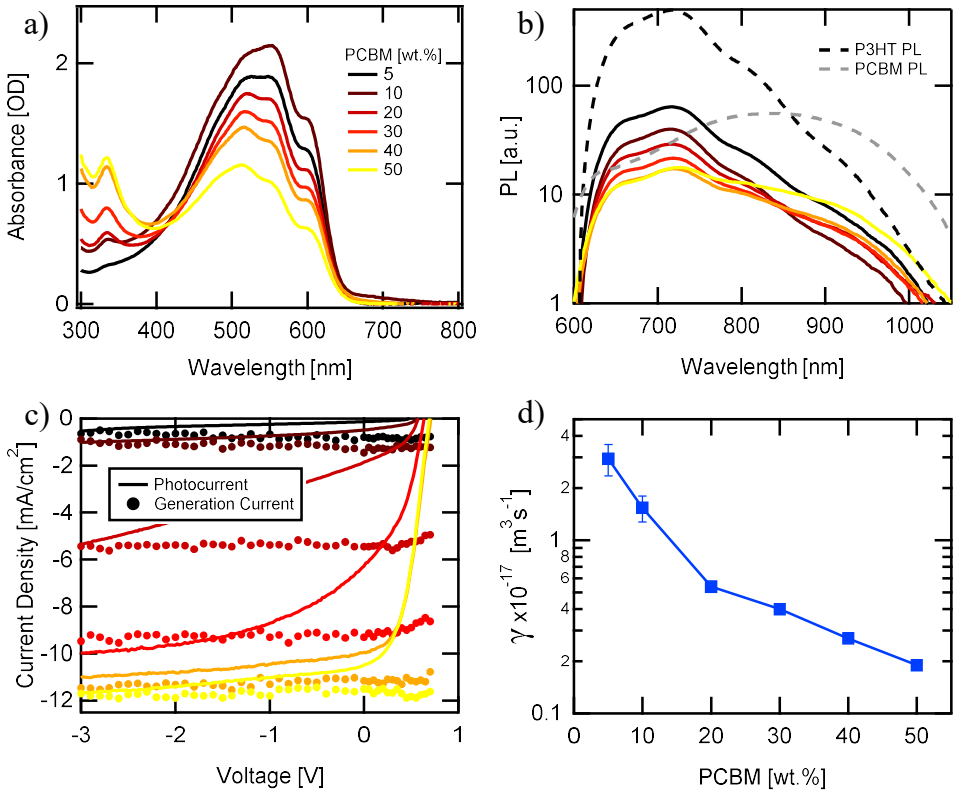

Figure 2: (a) UV-Vis absorption for all devices. Legend colors additionally apply to (b) and (c). (b) Thickness normalized photoluminescence spectra of devices with pure films of P3HT and PCBM for reference. (c) Measured photocurrent and voltage dependent generation current $J_{gen}(V)$ for all devices. Excitation wavelength was 550nm with a fluence of $0.27\mu J/cm^2$. (d) Bi-molecular recombination rate as a function of PCBM wt.% (uncertainties from fits to transients). Fits shown in the Supporting Information.

measurements[29,30] where here, we find that even devices with as low as 5 wt.% PCBM exhibit charge separation that is independent of field. Although the generation current is independent of field, it increases dramatically as a function of PCBM concentration. Since the total number of generated CT states is nearly identical in all devices, this result indicates that an increased efficiency of CT-state separation is one mechanism responsible for the higher short circuit current.

Charge generation independent of applied electric field implies a considerable component of device fill factor is due to bimolecular recombination. We can investigate the rate at which this occurs by varying t_d out to $10\mu s$, while holding a constant V_{pre} across the device equal to its max power point. This rate is quantified through fitting the extracted charge density n over time to a second order rate equation ($\frac{dn}{dt} = \gamma n^2$) using an iterative method developed by the Neher group.[30] γ is the bimolecular recombination coefficient. Data along with fits are given in the Figure S5 with γ presented in Figure 2d. We find that over the series investigated, γ decreases by more than an order of magnitude (~16x). Although TDCF may overestimate the magnitude of γ,[55] the overall trend will still be accurate. Additionally, the coefficient is not enough by itself to determine the impact of bimolecular recombination on device performance. It must be combined with the overall charge density (n) present in the devices and the average extraction time for charges (dependent on active layer thickness and charge mobility) in order to calculate total charge recombination for each device.

Quantum efficiencies of the charge generation process. From our optoelectronic measurements, we can now calculate the quantum efficiency of each step in the charge generation process. Our absorbance and PLQ measurements determine the first two steps with efficiencies η_{abs} and η_{CT} as described above with their trends displayed in Figure 3a as a function of PCBM concentration. As discussed earlier both efficiencies are independent of blend ratio and stay above 80% and 90% respectively, ensuring that the total population of CT states available for charge separation is approximately the same for each device in our series.

To calculate the efficiency of separating the CT-states into free charges (η_{sep}), we first calculate the maximum

current density available under AM1.5G solar illumination ($J_{\max}$), which assumes a 100% quantum efficient conversion of all available photons within a chosen wavelength range into extracted charge. For our calculations (Figure S7), we consider light up to $650nm$ as determined by the bandgap of P3HT. We next use J_{max} and the prior efficiencies to calculate the density of generated CT states $J_{CT} = \eta_{Abs} \times \eta_{CT} \times J_{max}$. The efficiency of charge separation can be calculated through the ratio of the generation current to the CT state density: $\eta_{sep} = J_{gen}/J_{CT}$. Figure 3a reveals that increasing PCBM concentration from 5 wt.% to 50 wt.% dramatically increases the charge separation efficiency from 5% to 80%.

Lastly, we can calculate the efficiency of charge extraction by comparing the photocurrent under solar illumination to the generation current: $\eta_{ext}(V) = J_{ph}(V)/J_{gen}$.[31,56,57] This is shown for each device as a function of cell voltage in Figure 2c. The difference between these curves represents charge lost due to bimolecular recombination following charge separation.[31,58] This efficiency is plotted in Figure 3a for max power point conditions, where much like the separation efficiency, increasing PCBM wt.% increases η_{ext}, in this case from 10% to 70%. Data at short circuit is given in Figure S8 and while it keeps to the same trend we see a significant decrease in bimolecular recombination as expected. The ability to separate losses from geminate and bimolecular recombination at operational conditions (rather than at open circuit or short circuit) is uniquely enabled via TDCF.

While it may look like the extraction and separation efficiencies have a similar impact on photocurrent we note that at each successive step there is a different density of excited states. To reflect this, Figure 3b gives a representation of the device current density at each step for maximum power point conditions, where values are represented as the percentage of J_{max}. In this representation the geminate recombination (red region), dramatically decreases from 65% to 12.5% as PCBM is added to the blend, while bimolecular recombination (orange region) actually increases somewhat from 3.9% to 19.3%. Thus, it is clear that the trends in geminate recombination fully dominate device performance trends, and the main effect of increased PCBM concentrations on device performance is to increase CT-state separation (charge generation). It is striking that J_{SC}, FF, and γ do not track bimolecular recombination losses in the completed device. In fact, they exhibit an *opposite* trend. Bimolecular recombination losses actually *increasing* with PCBM concentration is due to the dramatic increase in charge density from increased generation overwhelming the decrease in γ. This is in contrast to previous reports claiming increased photocurrents are due primarily to reduced bimolecular recombination.[27,48,55] This critical distinction between charge generation and extraction is often blurred together in other photocurrent measurements and points to the power of our analysis method debuted here.

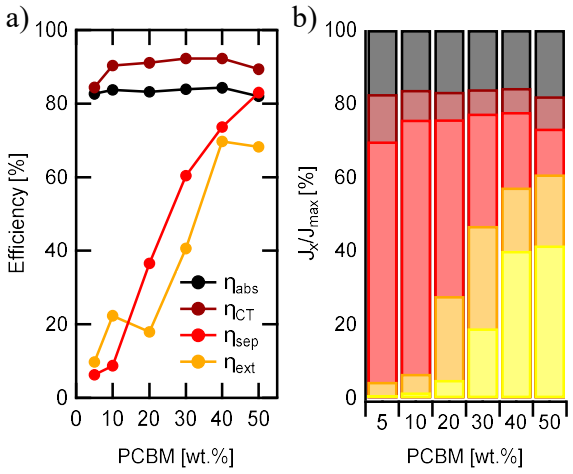

Figure 3: (a) Efficiency of each charge generation process as a function of PCBM wt.%. (b) Composite figure of charge density at each step in the process. From top to bottom, each colored region represents excited state populations relative to J_{max}: Photons not absorbed by the active layer (black), exciton recombination (maroon), geminate recombination (red), bimolecular recombination (orange), and charge extracted (yellow).

Device morphology. Having quantified the charge generation process, we next turn to quantify the device morphology with the goal of revealing the structural mechanisms behind the device behavior. RSoXS has been used extensively to reveal the nano-to-mesoscale domain structure within the active layer of an OPV[19,59–61] because the signal originates overwhelmingly from molecular contrast rather than electron density contrast. Lorentz-corrected RSoXS profiles of the measured OPV devices shown in Figure 4a are consistent with previous reports[16,62,63] with a single feature present at $q = 0.23nm^{-1}$, corresponding to a characteristic length of $l = 2\pi/q \approx 26nm$. This length is independent to PCBM wt.%, only varying over a range of $l = 24\ nm$ to $30\ nm$ in a non-monotonic fashion. Due to the static nature of this feature we interpret its origin to be the width of the pure P3HT crystalline fibrils[64] (form factor) rather than a distance between adjacent domains (structure factor), since swelling of PCBM domains between P3HT crystals would naturally increase such distances as seen in studies of other systems.[14,27] The upturn in scattering at $Q < 0.1\ nm^{-1}$ for PCBM concentrations of 40 and 50 wt.% was identified as surface roughness through spectral analysis (Figure S9). The profiles fit well to a rod form factor with a mean fibril radius of 9 nm (Figure S10), which is comparable to the exciton diffusion length for efficient exciton harvesting[65,66]

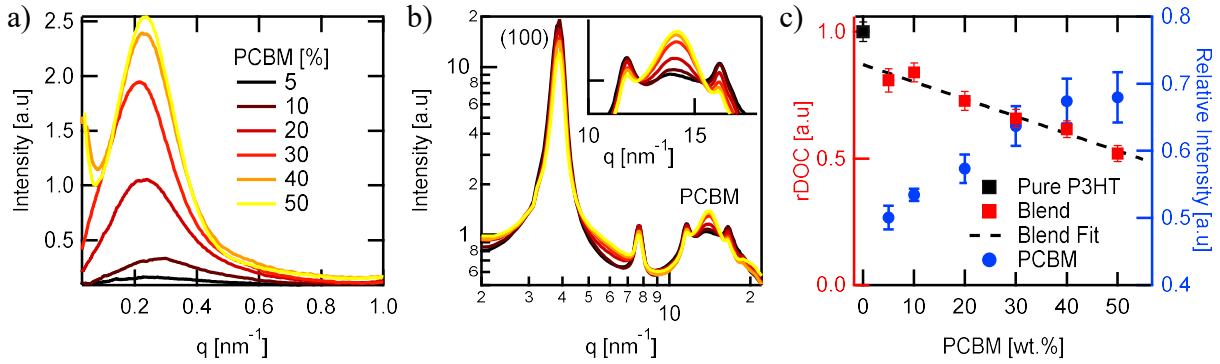

Figure 4: (a) Lorentz corrected RSoXS profiles taken at 283.5eV for each device. Legend colors additionally apply to (b). (b) Normalized circular averaged GIWAXS profiles. Data shown normalized at q=12.1nm^{-1}, but can also be normalized at several other q-values without significant changes. (c) P3HT (100) pole figure area (rDOC) and PCBM peak intensity as a function of PCBM wt.%. Uncertainties from possible normalization conditions. Dashed line is a linear fit is the blend P3HT rDOC.

evidenced by excellent PLQ in all PCBM concentrations (Figure 2b). We note that RSoXS primarily measured bulk average morphology and is insensitive to vertical segregation such as the wetting layers that are known to form within these devices.[67,68] However, due to the relatively large thickness of our active layers, the device dynamics will primarily originate from the structures measured by RSoXS.

Circularly averaged grazing incidence wide-angle X-ray scattering (GIWAXS) profiles are displayed in Figure 4b, which investigates the molecular packing and aggregation of both P3HT and PCBM. Peak identification for each is done through pure film scattering with all features in agreement with previous studies (Figure S12).[69–72] Relative degree of crystallinity (rDOC) from the P3HT (100) reflection allows a quantitative representation of the relative volume fraction occupied by the P3HT crystal (Figure S13).[53,73] Normalized rDOC is plotted in Figure 4c where increasing PCBM concentration in blends tracks a linear decrease in P3HT diffraction. The asymptotic trend in the blend films (dashed line) does not coincide with the measured signal from a pure P3HT film but is instead significantly lower. This indicates a lower P3HT crystallinity in the blends, likely due to an attractive interaction with PCBM molecules that lowers the free energy of crystallization.

The inset in Figure 4b focuses on the scattering feature from PCBM aggregates at $q = 13.9(1)\,nm^{-1}$. Peak fits (Figure S14 & S15) show only the 5 wt.% sample's peak position deviates to agree with the pure P3HT feature at $q = 13.5\,nm^{-1}$. The peak widths monotonically narrow with PCBM concentration, indicating increasing PCBM-PCBM correlation lengths. Additionally, Figure 4c presents the PCBM peak intensity, which exhibits a linear increase with PCBM concentration. Similar work conducted on other material systems have used the fullerene scattering peak intensity to identify the onset of PCBM aggregation into pure phases via a "constant-kink" concentration dependence.[74] Here, we do not see such a feature and can conclude that either a three-phase morphology exists throughout the device series, or the three-phase onset occurs at low PCBM wt.% such that it is obscured by the diffuse amorphous P3HT scattering.

Quantifying the mixed phase: Of keen interest here is the volume and composition of the interfacial mixed phase versus the pure phases (i.e. the state of the 3-phase system). The RSoXS profiles in Figure 4a reveal a gradual increase in scattering intensity with PCBM concentration, which is traditionally interpreted as an increase in domain purity in a two-phase system.[15,26] However, domain volume fractions also affect the scattering intensity but are commonly assumed to remain constant[36–39]. In a three-phase system, the situation is even more ambiguous with all phase volume fractions and their molecular compositions potentially changing. With the case of semicrystalline polymer-fullerene blends investigated here, the three phases are an amorphous mixed phase between a pure polymer crystal phase and a pure fullerene aggregate phase.[15–17] This results in three independent parameters: Volume fractions ϕ of two phases (the third adding to one) and the composition x of the mixed phase. Thus, there is likely a shift of both domain compositions and volume fractions. With three independent parameters determining the state of the system, we require three measurements.

A recent study measured the state of the system on a small-molecule OPV blend using GIWAXS measurements with the intensities fit to a two phase model (pure donor crystal and pure fullerene aggregate).[34] The deviation of the fit from the blend ratio revealed the third mixed phase. Two assumptions in the analysis were, first, that scaling the diffraction of a blend film would result in that of a pure film and, second, that a pure film would be 100% crystalline. Our rDOC results in Figure 4c show that the diffraction intensity of a blend film does not always asymptotically reach that of the pure film. Furthermore, most pure films are only semicrystalline, and some

independent measurement of absolute crystallinity for the pure film is necessary for a quantitative analysis. Fortunately, work by Snyder *et al.* has measured the absolute crystallinity of our donor polymer utilizing differential scanning calorimetry focusing on the properties of high molecular weight P3HT similar to that used in this study.[75] Correcting this measurement with differences in regioregularity[76] and differences in the asymptotic diffraction intensity of blended P3HT with that of pure P3HT (line in Figure 4c), we determined the absolute crystallinity of our blends to be $f_{wt} = 0.51$. (The absolute crystallinity of the pure film was calculated as $f_{wt} = 0.58$.) Here, f_{wt} is the weight fraction of crystal to total P3HT, the remainder being amorphous polymer. This value of absolute crystallinity is consistent with the linear trend measured for all blend devices suggesting that all samples have ~51 wt.% P3HT crystallinity.

Despite quantifying the absolute crystallinity of the donor material in our devices (i.e. the volume fraction of the pure donor phase ϕ_p), this measurement alone is not enough to quantify the state of the three phase system. To do this, we combine this measurement with two others: the overall donor-acceptor blend ratio and the total scattering intensity (TSI) measured by RSoXS. The TSI is an integration of measured scattering intensity across all of reciprocal space and through Porod Invariant formalism can be expressed in the following equation:[40,77]

$$TSI = \alpha \sum_{i \neq j} \left|\Delta x_{ij}\right|^2 \phi_i \phi_j \qquad (1)$$

where α is a term that is constant between all devices, $\left|\Delta x_{ij}\right|^2$ is the difference in molecular composition by mass between domains i and j, and ϕ_i is the volume fraction of domain i. (See SI for details.) In our three-phase model, the two remaining independent parameters are the volume fraction and composition of the mixed phase: ϕ_m and x_m, respectively.

Figure 5a displays the measured TSI as a function of PCBM concentration along with the model fit. $|\chi|^2 = 1.4$ for this fit, indicating it describes the data well. Resulting fit parameters (volume fractions and mixed phase molecular composition) are plotted as a function of PCBM concentration in Figure 5b. We find that at less than 8 wt.% total PCBM in the blend, the film exhibits the scattering behavior of a two-phase morphology where additional fullerene is miscible within the amorphous mixed phase. Once the mixed phase reaches a composition of 14.4 ± 0.8 wt.% PCBM, fullerene begins to aggregate into a third domain. This maximum composition is consistent with that of previous thermodynamic miscibility measurements of P3HT and PCBM[78,79] and indicates the devices reached an equilibrium state during film formation. As PCBM is further added to the blend, both volumes of the P3HT crystal phase and the mixed phase shrink. The highest

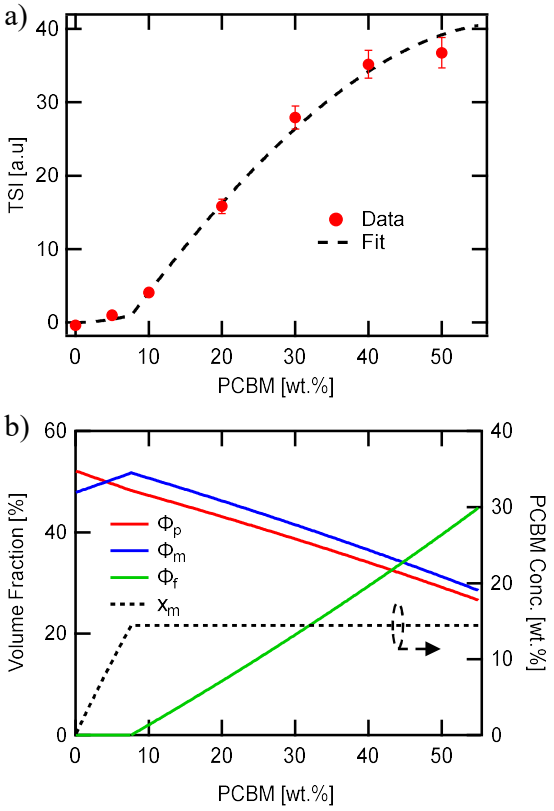

Figure 5: (a) Total scattering intensity as a function of PCBM wt.% along with model fit. A constant background has been removed from the data, which sets the TSI at 0 wt.% PCBM to zero. Uncertainties from incident beam intensity. (b) Volume fraction extracted from model fit as a function of PCBM wt.% and labels are the same as discussed in the main text. Mixed phase composition (dashed) gives the wt. % of PCBM within the mixed phase with the remaining mass consisting of amorphous P3HT.

performing cells around 40 and 50 wt.% PCBM have nearly balanced phase volume fractions. It is of note that a kink in the RSoXS TSI denotes a transition between two and three phases, but a kink is not seen in the PCBM GIWAXS scattering intensity, indicating that the backgrounds at the q-values investigated obscure the measurement. To the best of our knowledge this is the first time the three-phase morphology has been solved quantitatively. This critically required the enhanced sensitivity of RSoXS but could be conducted on any material system, including non-fullerene systems or even ternary systems with the use of our recently developed spectral analysis.[44]

The final result is that as PCBM is added to the blend, the aggregate phase volume increases while the mixed phase volume goes down. This is in good agreement with our PL spectroscopy measurements in Figure 2b, showing increasing fullerene exciton recombination, which can only result from a pure fullerene phase of the size scale near and above the exciton diffusion length. Additionally,

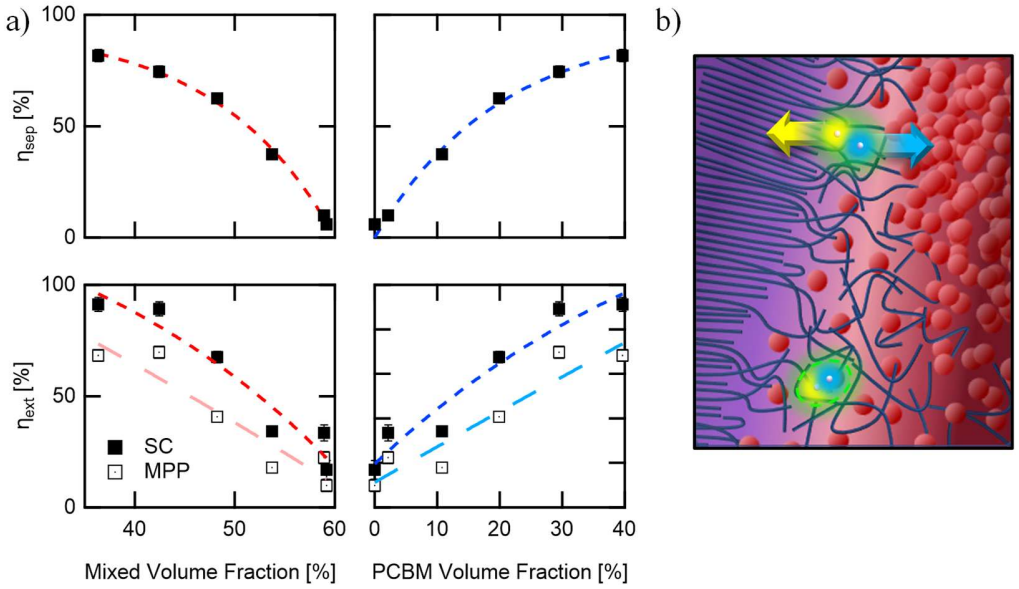

Figure 6: (a) Separation and extraction efficiency as functions of the mixed and pure PCBM volume fraction. Legend applies to all sub-graphs. Colored curves for η_{sep} are fits to equation 2 while those for η_{ext} are second order polynomials acting as guides to the eye. In lower panels, light colors are fits to efficiencies at max power point (MPP) rather than short circuit conditions (SC). (b) Schematic representation of the volume fraction distribution affecting the donor-acceptor interfacial width and therefore the charge separation efficiency. Yellow hole and blue electron at the top will separate while the pair at the bottom combines geminately due to lack of proximity to the pure fullerene aggregate phase.

the fullerene scattering peak width in Figure 4b monotonically decreases with increasing PCBM concentration, which is consistent with an increasing presence and organization of a pure fullerene phase. The peak position shifting to agree with that of pure P3HT at 5 wt.% PCBM further strengthens our analysis that no pure PCBM phase exists at this concentration but is instead in a two-phase state.

Impact of mixed and pure phases. Having quantified both the charge generation process and the phase volumes, we can directly relate the two within our devices. Figure 6a displays both the charge separation efficiency and extraction efficiency plotted against the mixed and pure PCBM phase volumes. Both efficiencies simultaneously anticorrelate with the mixed phase volume fraction and correlate with that of the pure PCBM phase. In particular, the separation efficiency fits well to a two-parameter exponential saturation model of the following form:

$$\eta_{sep} = A\left(1 - e^{-\phi/B}\right) \quad (2).$$

The fits reveal $A = \eta_{sep}^{max} = 96 \pm 8\%$ and $B = 20 \pm 4\ vol.\%$. The latter is the minimum volume fraction occupied by a pure PCBM phase required for efficient charge separation. Impressively, the graphs linearize when plotting $\ln\left(1 - \eta_{sep}/\eta_{max}\right)$ versus the pure and mixed volume fractions to yield a better than 99% Pearson correlation (Figure S16). Such an unprecedented quantitative structure-property correlation is likely due to the fact that RSoXS morphology experiments were conducted directly on the device films themselves without using duplicate samples, thus eliminating sample-to-sample variations.

Since the mixed phase occurs predominantly at the interface between pure domains,[16,17] this correlation indicates that a large mixed phase volume, and correspondingly a wide interface between pure phases, reduces CT state separation efficiency. Instead, close proximity of a CT state to a pure fullerene phase is necessary for efficient charge separation. We schematically propose this concept in Figure 6b where the presence of a large mixed phase becomes a source of geminate recombination, while a relatively narrow mixed interface between pure phases enhances separation efficiency of local CT states. We postulate that the aggregation of donor and acceptor molecules in pure phases proximate to the interface is the governing mechanism behind the separation efficiencies we measure here. In fact, the large (>100 meV) increase in V_{OC} from 5 to 10 wt.% PCBM without an increase in charge density (η_{sep}) not only solidifies our assertion that the pure PCBM phase is established at this concentration but also that it is present at and directly affects the donor-acceptor interface. The delayed improvement of J_{SC} and FF may come from the need for the pure PCBM phase to fully intercalate between P3HT fibrils, which requires a higher phase volume for efficient percolation of charges to electrodes.[80]

This is in line with studies that correlate overall device performance with aggregation of either donor or acceptor.[81–83] However, to our knowledge this is the first time such a correlation is made directly and quantitatively between charge separation efficiency and phase volume fractions. It is interesting to note that this is a different result than our recent study of small-molecule donor-based OPVs, where instead a large mixed phase correlated with increased charge generation and extraction.[22] In that case, however, we found donor alignment and aggregation occurring even in mixed phases, and that a lack of polymer tie chains between small molecule crystals may, in fact, require mixed phases at compositions that allow for charge percolation – a requirement unique to small-molecule OPVs.The strong correlation measured here further implies a causal relationship because other possible competing effects are accounted for in our analysis. For example, the efficiency of CT state generation (η_{CT}) does not track with the mixed phase volume fraction. The CT state density is, in fact, held constant in our study (~75%), while the mixed phase volume is cut roughly in half to 30 from 55 vol.%, This implies that the volume of the mixed phase is not important for CT state generation in this system. Another possibly contributing factor to the correlation – bimolecular recombination – is removed by our analysis as all charges are extracted at internal fields greater than $10^7 V/m$ and within 200 ns of generation. The extraction efficiency itself, while still moderately correlated with phase volume, shows a more scattered dependence compared to the separation efficiency, possibly due to charge mobility or film thickness effects. However, this moderate dependency supports previous studies that find increased molecular mixing correlated with lower FF.[15,40] A final potentially competing influence is polymer crystallinity. However, our rDOC measurement clearly shows a decreasing level with PCBM concentration – opposite the trend in η_{sep}. Put together, our control for contributing effects strongly indicates that the mixed phase interface is the dominant causal factor in determining the separation efficiency in our series.

While we do not altogether rule out the utility of a mixed phase interface for efficient polymer-based devices, we propose that the interfacial width between pure domains must be limited to enable both high charge separation efficiencies and continuous percolation pathways within the pure phases for charge extraction. This would result both in a high energetic gradient across the interface[33,45–47] as well as close proximity of delocalized charge states that exist in pure phases[84–86] – two possible mechanisms for the enhanced efficiency. As P3HT is a model semicrystalline polymer, this relationship is expected to be applicable in other high-performing semicrystalline polymers such as FTAZ, PGeBTBT, or PffBT4T,[37,41,42] and even apply to systems that include non-fullerene acceptors. In addition, this relationship should inform on the design of future polymeric systems. Donor-acceptor molecules designed with a high enthalpic cost of mixing (high interaction parameter) thus would be one target for high efficiency with such correlations recently noted.[15,40] By combining these morphological insights with recent advances in energy-level tuning and increased charge mobility, power conversion efficiencies of 20% appear feasible.

■ CONCLUSION

We presented a characterization of the step-by-step quantum efficiencies of power generation in model OPV devices simultaneous to the quantification of phase volume fraction, molecular composition/crystallinity, and nanodomain size. Increasing the overall PCBM concentration in the device resulted in a transition between two and three phases, where the compositional saturation of the amorphous mixed phase resulted in the appearance and growth of a third pure PCBM aggregate phase. We found that photon absorption and CT state generation is largely invariant to phase evolution primarily due to the self-limiting domain size appearing in the semicrystalline polymer. A moderate correlation is found between charge extraction and the pure phase volume, in agreement with previous results. However, an unprecedented >99% correlation between CT state separation efficiency (charge generation) and phase volume fraction – along with our ability to eliminate other possible factors – is the strongest evidence to date of a causal relationship between the pure aggregate phase and charge generation. A narrow mixed phase interfacial width between pure domains allows for CT states to more efficiently separate into free charges due to the steeper energetic gradient as well as the proximity to delocalized states in the pure phases. These results point to an increasingly focused ideal morphology in organic solar cells, consisting of a limited mixed phase between pure donor/acceptor domains supporting charge separation and extraction. The methods here are poised to study high performing materials or device concepts such as non-fullerene acceptors or ternary systems to generalize the role of the mixed phase in OPVs.

■ METHODS

Device Preparation and Performance. Pre-patterned ITO on glass substrates (145(10) nm, 20(2) Ωsq, 88% trans. @ 550 nm, NIST mask #550, Thin Film Devices) were first sonicated in sequential baths of detergent, water, acetone, and isopropyl alcohol and then treated to 15 min. of UV-ozone. Subsequently, substrates were coated with a PEDOT:PSS (Clevios P VP AI 4083, Heraeus) hole transport layer. Devices were next transferred into a nitrogen glovebox (O_2 & H_2O ~0.1 ppm) for the remainder of fabrication and device testing. Active layer solutions were made by co-dissolving

P3HT (Mw=50-70k, RR=91-94%, <0.01% metals, 4002-EE Rieke Metals) and PCBM (Nano-C) in dichlorobenzene with blend ratios of 5, 10, 20, 30, 40, and 50 wt.% PCBM. Total solid concentrations were varied from 30-45 g/l to make $\approx 300nm$ thick films. Solutions were spun-cast (800 RPM for 10s) and left to dry (>10min) before being transferred to a vacuum chamber for electrode deposition (20nm Ca / 150nm Al) via thermal evaporation (NexDep Angstrom Engineering), which resulted in four symmetric devices on each substrate with areas of 4 mm^2. Devices were not thermally annealed. J-V characterization (Keithley 2450) was conducted under AAA 1-sun illumination (Oriel 300W Xenon lamp with AM1.5G filter) at $1000W/m^2$ calibrated with a NIST-calibrated silicon photodiode (Thorlabs). Characteristics reported are averaged from four devices fabricated from a single thin film to ensure morphology is consistent across the substrate for subsequent X-ray measurements.

Absorption & Photoluminescence Spectroscopy. UV-Vis was conducted on device active layers before electrode deposition. Reference films of P3HT and PCBM were spuncast on PEDOT:PSS coated glass substrates following procedures for active layer fabrication. To simulate fullerene in a polymer matrix, PCBM reference films were cast in blends of polystyrene as done previously.[87] All visible light spectroscopy was measured with an Ocean Optics QEPro spectrometer cooled to $-25°C$. A cosine corrector (Thorlabs) was fiber coupled to spectrometer for photoluminescence (PL) to compare reference film and device emission intensities. PL excitation was carried out at a wavelength of $550nm$ (Ekspla NT232) with a 600 nm long-pass filter after the sample to block the laser excitation.

Time Delayed Collection Field. TDCF was carried out on the same devices and probe station for J-V testing with procedures similar to previous reports.[29,30] Excitation is accomplished with an ND-YAG pumped OPO (Ekspla NT232) with a 3 ns pulse width running at 100 Hz. To limit sample degradation and maximize throughput, laser light is fiber coupled onto the JV testing stage within the glovebox. Collection voltage was supplied through a custom amplification circuit synched with the laser pulse using a 250 MHz bandwidth function generator (Tektronix AFG 3251). Photocurrent transients are measured with a 12-bit, 1 GHz bandwidth oscilloscope (Teledyne LeCroy HDO 4104).

X-ray Scattering. RSoXS was conducted at beamline 11.0.1.2 at the ALS.[88] Active layers of the actual devices tested were released from the substrate by dissolving the PEDOT:PSS layer in deionized water with the floating active layers picked up on silicon nitride windows (Norcada). Procedures for the experiment have been published previously with enhanced q-range obtained by varying the sample-detector distances.[89] For accurate relative scattering intensities between samples, it was necessary to calibrate incident beam intensity every other sample to counter beam drift.[44] Samples for X-ray diffraction were prepared on Na:PSS coated silicon substrates with processing conditions identical to device fabrication. Experiments were carried out at beamline 7.3.3 at the Advanced Light Source (ALS)[90] and all results were measured at grazing incidence with angle of $0.2°$ (above the critical angle for sample and substrate). All X-ray data reduction was done through the IGOR package NIKA by Jan Ilavsky[91] with a custom skin used to process RSoXS.[92]

■ ASSOCIATED CONTENT

Supporting Information. Details regarding JV device metrics, transfer matrix modeling, calculations for PLQ and generation current, delay dependent TDCF results and model fits, maximum current calculation, quantum efficiencies at short circuit current, off-resonant scattering with contrast functions, form-factor scattering models, device thickness measurements, pure sample GIWAXS, P3HT (100) pole figure analysis, multi-peak fitting for PCBM GIWAXS feature, TSI scattering model details, correlation analysis.

■ AUTHOR INFORMATION

Corresponding Author
brian.collins@wsu.edu

Notes
The authors declare no competing financial interests.

■ ACKNOWLEDGEMENTS

The authors gratefully acknowledge help in designing the TDCF setup from Jona Kurpiers and Dieter Neher. T. Ferron was financially supported by U.S. Department of Energy, Office of Science, Basic Energy Sciences, Early Career Research Award number DE-SC0017923. This research used resources of the Advanced Light Source, which is a DOE Office of Science User Facility under contract no. DE-AC02-05CH11231.

■ REFERENCES

(1) Krebs, F. C. Fabrication and Processing of Polymer Solar Cells: A Review of Printing and Coating Techniques. *Sol. Energy Mater. Sol. Cells* **2009**, *93* (4), 394–412.

(2) Søndergaard, R. R.; Hösel, M.; Krebs, F. C. Roll-to-Roll Fabrication of Large Area Functional Organic Materials. *J. Polym. Sci. Part B Polym. Phys.* **2013**, *51* (1), 16–34.

(3) Liang, Y.; Feng, D.; Wu, Y.; Tsai, S. T.; Li, G.; Ray, C.; Yu, L. Highly Efficient Solar Cell Polymers Developed via Fine-Tuning of Structural and Electronic Properties. *J. Am. Chem. Soc.* **2009**, *131* (22), 7792–7799.

(4) Lipomi, D. J.; Chong, H.; Vosgueritchian, M.; Mei, J.; Bao, Z. Toward Mechanically Robust and Intrinsically Stretchable Organic Solar Cells: Evolution of Photovoltaic Properties with Tensile

Strain. *Sol. Energy Mater. Sol. Cells* **2012**, *107*, 355–365.

(5) Forberich, K.; Guo, F.; Bronnbauer, C.; Brabec, C. J. Efficiency Limits and Color of Semitransparent Organic Solar Cells for Application in Building-Integrated Photovoltaics. *Energy Technol.* **2015**, *3* (10), 1051–1058.

(6) Li, S.; Ye, L.; Zhao, W.; Yan, H.; Yang, B.; Liu, D.; Li, W.; Ade, H.; Hou, J. A Wide Band-Gap Polymer with a Deep HOMO Level Enables 14.2% Efficiency in Polymer Solar Cells. *J. Am. Chem. Soc.* **2018**, *140*, 7159–7167.

(7) Zhang, S.; Qin, Y.; Zhu, J.; Hou, J. Over 14% Efficiency in Polymer Solar Cells Enabled by a Chlorinated Polymer Donor. *Adv. Mater.* **2018**, *30* (20), 1–7.

(8) Meng, L.; Zhang, Y.; Wan, X.; Li, C.; Zhang, X.; Wang, Y.; Ke, X.; Xiao, Z.; Ding, L.; Xia, R.; et al. Organic and Solution-Processed Tandem Solar Cells with 17.3% Efficiency. *Science (80-.).* **2018**.

(9) Janssen, R. A. J.; Nelson, J. Factors Limiting Device Efficiency in Organic Photovoltaics. *Adv. Mater.* **2013**, *25* (13), 1847–1858.

(10) Baran, D.; Kirchartz, T.; Wheeler, S.; Dimitrov, S.; Abdelsamie, M.; Gorman, J.; Ashraf, R. S.; Holliday, S.; Wadsworth, A.; Gasparini, N.; et al. Reduced Voltage Losses Yield 10% Efficient Fullerene Free Organic Solar Cells with >1 V Open Circuit Voltages. *Energy Environ. Sci.* **2016**, *9* (12), 3783–3793.

(11) Huang, Y.; Kramer, E. J.; Heeger, A. J.; Bazan, G. C. Bulk Heterojunction Solar Cells: Morphology and Performance Relationships. *Chem. Rev.* **2014**, *114* (14), 7006–7043.

(12) Collins, B. A.; Tumbleston, J. R.; Ade, H. Miscibility, Crystallinity, and Phase Development in P3HT/PCBM Solar Cells: Toward an Enlightened Understanding of Device Morphology and Stability. *J. Phys. Chem. Lett.* **2011**, *2* (24), 3135–3145.

(13) Chen, D.; Nakahara, A.; Wei, D.; Nordlund, D.; Russell, T. P. P3HT/PCBM Bulk Heterojunction Organic Photovoltaics: Correlating Efficiency and Morphology. *Nano Lett.* **2011**, *11* (2), 561–567.

(14) Tumbleston, J. R.; Yang, L.; You, W.; Ade, H. Morphology Linked to Miscibility in Highly Amorphous Semi-Conducting Polymer/Fullerene Blends. *Polym. (United Kingdom)* **2014**, *55* (19), 4884–4889.

(15) Ye, L.; Hu, H.; Ghasemi, M.; Wang, T.; Collins, B. A.; Kim, J. H.; Jiang, K.; Carpenter, J. H.; Li, H.; Li, Z.; et al. Quantitative Relations between Interaction Parameter, Miscibility and Function in Organic Solar Cells. *Nat. Mater.* **2018**, *17* (3), 253–260.

(16) Guo, C.; Kozub, D. R.; Vajjala Kesava, S.; Wang, C.; Hexemer, A.; Gomez, E. D. Signatures of Multiphase Formation in the Active Layer of Organic Solar Cells from Resonant Soft X-Ray Scattering. *ACS Macro Lett.* **2013**, *2* (3), 185–189.

(17) Pfannmöller, M.; Flügge, H.; Benner, G.; Wacker, I.; Sommer, C.; Hanselmann, M.; Schmale, S.; Schmidt, H.; Hamprecht, F. A.; Rabe, T.; et al. Visualizing a Homogeneous Blend in Bulk Heterojunction Polymer Solar Cells by Analytical Electron Microscopy. *Nano Lett.* **2011**, *11* (8), 3099–3107.

(18) Vandewal, K.; Himmelberger, S.; Salleo, A. Structural Factors That Affect the Performance of Organic Bulk Heterojunction Solar Cells. *Macromolecules* **2013**, *46* (16), 6379–6387.

(19) Mukherjee, S.; Proctor, C. M.; Bazan, G. C.; Nguyen, T. Q.; Ade, H. Significance of Average Domain Purity and Mixed Domains on the Photovoltaic Performance of High-Efficiency Solution-Processed Small-Molecule BHJ Solar Cells. *Adv. Energy Mater.* **2015**, *5* (21), 1–11.

(20) Mukherjee, S.; Proctor, C. M.; Tumbleston, J. R.; Bazan, G. C.; Nguyen, T. Q.; Ade, H. Importance of Domain Purity and Molecular Packing in Effi Cient Solution-Processed Small-Molecule Solar Cells. *Adv. Mater.* **2015**, *27* (6), 1105–1111.

(21) Treat, N. D.; Varotto, A.; Takacs, C. J.; Batara, N.; Al-Hashimi, M.; Heeney, M. J.; Heeger, A. J.; Wudl, F.; Hawker, C. J.; Chabinyc, M. L. Polymer-Fullerene Miscibility: A Metric for Screening New Materials for High-Performance Organic Solar Cells. *J. Am. Chem. Soc.* **2012**, *134* (38), 15869–15879.

(22) Alqahtani, O.; Babics, M.; Gorenflot, J.; Savikhin, V.; Ferron, T.; Balawi, A. H.; Paulke, A.; Kan, Z.; Pope, M.; Clulow, A. J.; et al. Mixed Domains Enhance Charge Generation and Extraction in Bulk-Heterojunction Solar Cells with Small-Molecule Donors. *Advanced Energy Materials*. 2018, pp 1–16.

(23) Buchaca-Domingo, E.; Ferguson, A. J.; Jamieson, F. C.; McCarthy-Ward, T.; Shoaee, S.; Tumbleston, J. R.; Reid, O. G.; Yu, L.; Madec, M. B.; Pfannmöller, M.; et al. Additive-Assisted Supramolecular Manipulation of Polymer:Fullerene Blend Phase Morphologies and Its Influence on Photophysical Processes. *Mater. Horizons* **2014**, *1* (2), 270–279.

(24) Dou, F.; Buchaca-Domingo, E.; Sakowicz, M.; Rezasoltani, E.; McCarthy-Ward, T.; Heeney, M.; Zhang, X.; Stingelin, N.; Silva, C. The Effect of Phase Morphology on the Nature of Long-Lived Charges in Semiconductor Polymer:Fullerene Systems. *J. Mater. Chem. C* **2015**, *3* (15), 3722–3729.

(25) Scarongella, M.; De Jonghe-Risse, J.; Buchaca-Domingo, E.; Causa, M.; Fei, Z.; Heeney, M.; Moser, J. E.; Stingelin, N.; Banerji, N. A Close Look at Charge Generation in Polymer: Fullerene Blends with Microstructure Control. *J. Am. Chem. Soc.* **2015**, *137* (8), 2908–2918.

(26) Ye, L.; Collins, B. A.; Jiao, X.; Zhao, J.; Yan, H.; Ade, H. Miscibility-Function Relations in Organic Solar Cells: Significance of Optimal Miscibility in

Relation to Percolation. *Adv. Energy Mater.* **2018**, *1703058*, 1703058.

(27) Huang, W.; Gann, E.; Chandrasekaran, N.; Thomsen, L.; Prasad, S. K. K.; Hodgkiss, J. M.; Kabra, D.; Cheng, Y. B.; McNeill, C. R. Isolating and Quantifying the Impact of Domain Purity on the Performance of Bulk Heterojunction Solar Cells. *Energy Environ. Sci.* **2017**, *10* (8), 1843–1853.

(28) Gorenflot, J.; Paulke, A.; Piersimoni, F.; Wolf, J.; Kan, Z.; Cruciani, F.; Labban, A. El; Neher, D.; Beaujuge, P. M.; Laquai, F. From Recombination Dynamics to Device Performance: Quantifying the Efficiency of Exciton Dissociation, Charge Separation, and Extraction in Bulk Heterojunction Solar Cells with Fluorine-Substituted Polymer Donors. *Adv. Energy Mater.* **2018**, *8* (4), 1–12.

(29) Kniepert, J.; Lange, I.; Van Der Kaap, N. J.; Koster, L. J. A.; Neher, D. A Conclusive View on Charge Generation, Recombination, and Extraction in as-Prepared and Annealed P3HT:PCBM Blends: Combined Experimental and Simulation Work. *Adv. Energy Mater.* **2014**, *4* (7).

(30) Kniepert, J.; Schubert, M.; Blakesley, J.; Neher, D. Photogeneration and Recombination in P3HT : PCBM Solar Cells Probed by Time Delayed Collection Field Experiments. *J. Phys. Chem. Lett.* **2011**, 700–705.

(31) Albrecht, S.; Janietz, S.; Schindler, W.; Frisch, J.; Kurpiers, J.; Kniepert, J.; Inal, S.; Pingel, P.; Fostiropoulos, K.; Koch, N.; et al. Fluorinated Copolymer PCPDTBT with Enhanced Open-Circuit Voltage and Reduced Recombination for Highly Efficient Polymer Solar Cells. *J. Am. Chem. Soc.* **2012**, *134* (36), 14932–14944.

(32) Kozub, D. R.; Vakhshouri, K.; Orme, L. M.; Wang, C.; Hexemer, A.; Gomez, E. D. Polymer Crystallization of Partially Miscible Polythiophene/Fullerene Mixtures Controls Morphology. *Macromolecules* **2011**, *44* (14), 5722–5726.

(33) Sweetnam, S.; Graham, K. R.; Ndjawa, G. O. N.; Heumüller, T.; Bartelt, J. A.; Burke, T. M.; Li, W.; You, W.; Amassian, A.; McGehee, M. D. Characterization of the Polymer Energy Landscape in Polymer : Fullerene Bulk Heterojunctions with Pure and Mixed Phases. *J. Am. Chem. Soc.* **2014**, *136* (Cv), 14078–14088.

(34) Oosterhout, S. D.; Savikhin, V.; Zhang, J.; Zhang, Y.; Burgers, M. A.; Marder, S. R.; Bazan, G. C.; Toney, M. F. Mixing Behavior in Small Molecule:Fullerene Organic Photovoltaics. *Chem. Mater.* **2017**, *29* (7), 3062–3069.

(35) Ruderer, M. A.; Meier, R.; Porcar, L.; Cubitt, R.; Müller-Buschbaum, P. Phase Separation and Molecular Intermixing in Polymer-Fullerene Bulk Heterojunction Thin Films. *J. Phys. Chem. Lett.* **2012**, *3* (6), 683–688.

(36) Lin, Y.; Zhao, F.; Wu, Y.; Chen, K.; Xia, Y.; Li, G.; Prasad, S. K. K.; Zhu, J.; Huo, L.; Bin, H.; et al. Mapping Polymer Donors toward High-Efficiency Fullerene Free Organic Solar Cells. *Adv. Mater.* **2017**, *29* (3).

(37) Ye, L.; Xiong, Y.; Zhang, Q.; Li, S.; Wang, C.; Jiang, Z.; Hou, J.; You, W.; Ade, H. Surpassing 10% Efficiency Benchmark for Nonfullerene Organic Solar Cells by Scalable Coating in Air from Single Nonhalogenated Solvent. *Adv. Mater.* **2018**, *30* (8), 1–9.

(38) Roland, S.; Yan, L.; Zhang, Q.; Jiao, X.; Hunt, A.; Ghasemi, M.; Ade, H.; You, W.; Neher, D. Charge Generation and Mobility-Limited Performance of Bulk Heterojunction Solar Cells with a Higher Adduct Fullerene. *J. Phys. Chem. C* **2017**, *121* (19), 10305–10316.

(39) Yao, H.; Li, Y.; Hu, H.; Chow, P. C. Y.; Chen, S.; Zhao, J.; Li, Z.; Carpenter, J. H.; Lai, J. Y. L.; Yang, G.; et al. A Facile Method to Fine-Tune Polymer Aggregation Properties and Blend Morphology of Polymer Solar Cells Using Donor Polymers with Randomly Distributed Alkyl Chains. *Adv. Energy Mater.* **2018**, *8* (6), 1–6.

(40) Ye, L.; Zhao, W.; Li, S.; Mukherjee, S.; Carpenter, J. H.; Awartani, O.; Jiao, X.; Hou, J.; Ade, H. High-Efficiency Nonfullerene Organic Solar Cells: Critical Factors That Affect Complex Multi-Length Scale Morphology and Device Performance. *Adv. Energy Mater.* **2017**, *7* (7), 1–10.

(41) Fei, Z.; Kym, J. S.; Smith, J.; Domingo, E. B.; Anthopoulos, T. D.; Stingelin, N.; Watkins, S. E.; Kim, J. S.; Heeney, M. A Low Band Gap Co-Polymer of Dithienogermole and 2,1,3-Benzothiadiazole by Suzuki Polycondensation and Its Application in Transistor and Photovoltaic Cells. *J. Mater. Chem.* **2011**, *21* (40), 16257–16263.

(42) Liu, Y.; Zhao, J.; Li, Z.; Mu, C.; Ma, W.; Hu, H.; Jiang, K.; Lin, H.; Ade, H.; Yan, H. Aggregation and Morphology Control Enables Multiple Cases of High-Efficiency Polymer Solar Cells. *Nat. Commun.* **2014**, *5* (9), 1–8.

(43) Collins, B. A.; Li, Z.; Tumbleston, J. R.; Gann, E.; Mcneill, C. R.; Ade, H. Absolute Measurement of Domain Composition and Nanoscale Size Distribution Explains Performance in PTB7:PC71bm Solar Cells. *Adv. Energy Mater.* **2013**, *3* (1), 65–74.

(44) Ferron, T.; Pope, M.; Collins, B. A. Spectral Analysis for Resonant Soft X-Ray Scattering Enables Measurement of Interfacial Width in 3D Organic Nanostructures. *Phys. Rev. Lett.* **2017**, *119* (16), 1–6.

(45) Groves, C. Suppression of Geminate Charge Recombination in Organic Photovoltaic Devices with a Cascaded Energy Heterojunction. *Energy Environ. Sci.* **2013**, *6* (6), 1546–1551.

(46) Burke, T. M.; McGehee, M. D. How High Local Charge Carrier Mobility and an Energy Cascade in a Three-Phase Bulk Heterojunction Enable >90% Quantum Efficiency. *Adv. Mater.* **2014**, *26* (12), 1923–1928.

(47) Mueller, C. J.; Brendel, M.; Ruckdeschel, P.; Pflaum, J.; Thelakkat, M. Diketopyrrolopyrroles with a Distinct Energy Level Cascade for Efficient Charge Carrier Generation in Organic Solar Cells. *Adv. Energy Mater.* **2015**, *5* (21), 1–10.

(48) Müller, C.; Ferenczi, T. A. M.; Campoy-Quiles, M.; Frost, J. M.; Bradley, D. D. C.; Smith, P.; Stingelin-Stutzmann, N.; Nelson, J. Binary Organic Photovoltaic Blends: A Simple Rationale for Optimum Compositions. *Adv. Mater.* **2008**, *20* (18), 3510–3515.

(49) Li, N.; MacHui, F.; Waller, D.; Koppe, M.; Brabec, C. J. Determination of Phase Diagrams of Binary and Ternary Organic Semiconductor Blends for Organic Photovoltaic Devices. *Sol. Energy Mater. Sol. Cells* **2011**, *95* (12), 3465–3471.

(50) Spano, F. C. Modeling Disorder in Polymer Aggregates: The Optical Spectroscopy of Regioregular Poly(3-Hexylthiophene) Thin Films. *J. Chem. Phys.* **2005**, *122* (23).

(51) Burkhard, G. F.; Hoke, E. T.; McGehee, M. D. Accounting for Interference, Scattering, and Electrode Absorption to Make Accurate Internal Quantum Efficiency Measurements in Organic and Other Thin Solar Cells. *Adv. Mater.* **2010**, *22* (30), 3293–3297.

(52) Sariciftci, N. S.; Smilowitz, L.; Heeger, A. J.; Wudl, F. Photoinduced Electron Transfer from a Conducting Polymer to Buckminsterfullerene. *Science (80-.).* **1992**, *258* (5087), 1474 LP-1476.

(53) Schubert, M.; Collins, B. A.; Mangold, H.; Howard, I. A.; Schindler, W.; Vandewal, K.; Roland, S.; Behrends, J.; Kraffert, F.; Steyrleuthner, R.; et al. Correlated Donor/Acceptor Crystal Orientation Controls Photocurrent Generation in All-Polymer Solar Cells. *Adv. Funct. Mater.* **2014**, *24* (26), 4068–4081.

(54) Arndt, A. P.; Gerhard, M.; Quintilla, A.; Howard, I. A.; Koch, M.; Lemmer, U. Time-Resolved Charge-Transfer State Emission in Organic Solar Cells: Temperature and Blend Composition Dependences of Interfacial Traps. *J. Phys. Chem. C* **2015**, *119* (24), 13516–13523.

(55) Heiber, M. C.; Okubo, T.; Ko, S.-J.; Luginbuhl, B. R.; Ran, N.; Wang, M.; Wang, H.; Uddin, M. A.; Woo, H. Y.; Bazan, G. C.; et al. Measuring the Competition between Bimolecular Charge Recombination and Charge Transport in Organic Solar Cells under Operating Conditions. *Energy Environ. Sci.* **2018**.

(56) Credgington, D.; Jamieson, F. C.; Walker, B.; Nguyen, T. Q.; Durrant, J. R. Quantification of Geminate and Non-Geminate Recombination Losses within a Solution-Processed Small-Molecule Bulk Heterojunction Solar Cell. *Adv. Mater.* **2012**, *24* (16), 2135–2141.

(57) Dibb, G. F. A.; Jamieson, F. C.; Maurano, A.; Nelson, J.; Durrant, J. R. Limits on the Fill Factor in Organic Photovoltaics: Distinguishing Nongeminate and Geminate Recombination Mechanisms. *J. Phys. Chem. Lett.* **2013**, *4* (5), 803–808.

(58) Proctor, C. M.; Albrecht, S.; Kuik, M.; Neher, D.; Nguyen, T. Q. Overcoming Geminate Recombination and Enhancing Extraction in Solution-Processed Small Molecule Solar Cells. *Adv. Energy Mater.* **2014**, *4* (10).

(59) Carpenter, J. H.; Hunt, A.; Ade, H. Characterizing Morphology in Organic Systems with Resonant Soft X-Ray Scattering. *J. Electron Spectros. Relat. Phenomena* **2015**, *200*, 2–14.

(60) Lee, C.; Li, Y.; Lee, W.; Lee, Y.; Choi, J.; Kim, T.; Wang, C.; Gomez, E. D.; Woo, H. Y.; Kim, B. J. Correlation between Phase-Separated Domain Sizes of Active Layer and Photovoltaic Performances in All-Polymer Solar Cells. *Macromolecules* **2016**, *49* (14), 5051–5058.

(61) Kurpiers, J.; Ferron, T.; Roland, S.; Jakoby, M.; Thiede, T.; Jaiser, F.; Albrecht, S.; Janietz, S.; Collins, B. A.; Howard, I. A.; et al. Probing the Pathways of Free Charge Generation in Organic Bulk Heterojunction Solar Cells. *Nat. Commun.* No. 2018, 1–11.

(62) Yin, W.; Dadmun, M. A New Model for the Morphology of P3ht/Pcbm Organic Photovoltaics from Small-Angle Neutron Scattering: Rivers and Streams. *ACS Nano* **2011**, *5* (6), 4756–4768.

(63) Liao, H.-C.; Tsao, C.-S.; Lin, T.-H.; Chuang, C.-M.; Chen, C.-Y.; Jeng, U.-S.; Su, C.-H.; Chen, Y.-F.; Su, W.-F. Quantitative Nanoorganized Structural Evolution for a High Efficiency Bulk Heterojunction Polymer Solar Cell. *J. Am. Chem. Soc.* **2011**, *133* (33), 13064–13073.

(64) Herzing, A. A.; Richter, L. J.; Anderson, I. M. 3D Nanoscale Characterization of Thin-Film Organic Photovoltaic Device Structures via Spectroscopic Contrast in the TEM. *J. Phys. Chem. C* **2010**, *114* (41), 17501–17508.

(65) Shaw, P. E.; Ruseckas, A.; Samuel, I. D. W. Exciton Diffusion Measurements in Poly(3-Hexylthiophene). *Adv. Mater.* **2008**, *20* (18), 3516–3520.

(66) Markov, D. E.; Amsterdam, E.; Blom, P. W. M.; Sieval, A. B.; Hummelen, J. C. Accurate Measurement of the Exciton Diffusion Length in a Conjugated Polymer Using a Heterostructure with a Side-Chain Cross-Linked Fullerene Layer. *J. Phys. Chem. A* **2005**, *109* (24), 5266–5274.

(67) Ruderer, M. A.; Guo, S.; Meier, R.; Chiang, H. Y.; Körstgens, V.; Wiedersich, J.; Perlich, J.; Roth, S. V.;

Müller-Buschbaum, P. Solvent-Induced Morphology in Polymer-Based Systems for Organic Photovoltaics. *Adv. Funct. Mater.* **2011**, *21* (17), 3382–3391.

(68) Parnell, A. J.; Dunbar, A. D. F.; Pearson, A. J.; Staniec, P. A.; Dennison, A. J. C.; Hamamatsu, H.; Skoda, M. W. A.; Lidzey, D. C.; Jones, R. A. L. Depletion of PCBM at the Cathode Interface in P3HT/ PCBM Thin Films as Quantified via Neutron Reflectivity Measurements. *Adv. Mater.* **2010**, *22* (22), 2444–2447.

(69) Gomez, E. D.; Barteau, K. P.; Wang, H.; Toney, M. F.; Loo, Y. L. Correlating the Scattered Intensities of P3HT and PCBM to the Current Densities of Polymer Solar Cells. *Chem. Commun.* **2011**, *47* (1), 436–438.

(70) Treat, N. D.; Brady, M. A.; Smith, G.; Toney, M. F.; Kramer, E. J.; Hawker, C. J.; Chabinyc, M. L. Interdiffusion of PCBM and P3HT Reveals Miscibility in a Photovoltaically Active Blend. *Adv. Energy Mater.* **2011**, *1* (1), 82–89.

(71) Verploegen, E.; Mondal, R.; Bettinger, C. J.; Sok, S.; Toney, M. F.; Bao, Z. Effects of Thermal Annealing upon the Morphology of Polymer-Fullerene Blends. *Adv. Funct. Mater.* **2010**, *20* (20), 3519–3529.

(72) Andersen, T. R.; Dam, H. F.; Hösel, M.; Helgesen, M.; Carlé, J. E.; Larsen-Olsen, T. T.; Gevorgyan, S. A.; Andreasen, J. W.; Adams, J.; Li, N.; et al. Scalable, Ambient Atmosphere Roll-to-Roll Manufacture of Encapsulated Large Area, Flexible Organic Tandem Solar Cell Modules. *Energy Environ. Sci.* **2014**, *7* (9), 2925–2933.

(73) Hammond, M. R.; Kline, R. J.; Herzing, A. A.; Richter, L. J.; Germack, D. S.; Ro, H. W.; Soles, C. L.; Fischer, D. A.; Xu, T.; Yu, L.; et al. Molecular Order in High-Efficiency Polymer/Fullerene Bulk Heterojunction Solar Cells. *ACS Nano* **2011**, *5* (10), 8248–8257.

(74) Bartelt, J. A.; Beiley, Z. M.; Hoke, E. T.; Mateker, W. R.; Douglas, J. D.; Collins, B. A.; Tumbleston, J. R.; Graham, K. R.; Amassian, A.; Ade, H.; et al. The Importance of Fullerene Percolation in the Mixed Regions of Polymer-Fullerene Bulk Heterojunction Solar Cells. *Adv. Energy Mater.* **2013**, *3* (3), 364–374.

(75) Snyder, C. R.; Nieuwendaal, R. C.; Delongchamp, D. M.; Luscombe, C. K.; Sista, P.; Boyd, S. D. Quantifying Crystallinity in High Molar Mass Poly(3-Hexylthiophene). *Macromolecules* **2014**, *47* (12), 3942–3950.

(76) Snyder, C. R.; Henry, J. S.; Delongchamp, D. M. Effect of Regioregularity on the Semicrystalline Structure of Poly(3-Hexylthiophene). *Macromolecules* **2011**, *44* (18), 7088–7091.

(77) Wu, W. Small-Angle X-Ray Study of Particulate Reinforced Composites. *Polymer (Guildf).* **1982**, *23* (13), 1907–1912.

(78) Collins, B. A.; Gann, E.; Guignard, L.; He, X.; McNeill, C. R.; Ade, H. Molecular Miscibility of Polymer-Fullerene Blends. *J. Phys. Chem. Lett.* **2010**, *1* (21), 3160–3166.

(79) Chen, H.; Hegde, R.; Browning, J.; Dadmun, M. D. The Miscibility and Depth Profile of PCBM in P3HT: Thermodynamic Information to Improve Organic Photovoltaics. *Phys. Chem. Chem. Phys.* **2012**, *14* (16), 5635–5641.

(80) Vakhshouri, K.; Kozub, D. R.; Wang, C.; Salleo, A.; Gomez, E. D. Effect of Miscibility and Percolation on Electron Transport in Amorphous Poly(3-Hexylthiophene)/Phenyl-C 61-Butyric Acid Methyl Ester Blends. *Phys. Rev. Lett.* **2012**, *108* (2), 1–5.

(81) Menke, S. M.; Cheminal, A.; Conaghan, P.; Ran, N. A.; Greehnam, N. C.; Bazan, G. C.; Nguyen, T. Q.; Rao, A.; Friend, R. H. Order Enables Efficient Electron-Hole Separation at an Organic Heterojunction with a Small Energy Loss. *Nat. Commun.* **2018**, *9* (1), 1–7.

(82) Jamieson, F. C.; Domingo, E. B.; McCarthy-Ward, T.; Heeney, M.; Stingelin, N.; Durrant, J. R. Fullerene Crystallisation as a Key Driver of Charge Separation in Polymer/Fullerene Bulk Heterojunction Solar Cells. *Chem. Sci.* **2012**, *3* (2), 485–492.

(83) Veldman, D.; Ipek, Ö.; Meskers, S. C. J.; Sweelssen, J.; Koetse, M. M.; Veenstra, S. C.; Kroon, J. M.; Van Bavel, S. S.; Loos, J.; Janssen, R. A. J. Compositional and Electric Field Dependence of the Dissociation of Charge Transfer Excitons in Alternating Polyfluorene Copolymer/Fullerene Blends. *J. Am. Chem. Soc.* **2008**, *130* (24), 7721–7735.

(84) Bakulin, A. A.; Rao, A.; Pavelyev, V. G.; van Loosdrecht, P. H. M.; Pshenichnikov, M. S.; Niedzialek, D.; Cornil, J.; Beljonne, D.; Friend, R. H. The Role of Driving Energy and Delocalized States for Charge Separation in Organic Semiconductors. *Science (80-.).* **2012**, *335* (6074), 1340 LP-1344.

(85) Feier, H. M.; Reid, O. G.; Pace, N. A.; Park, J.; Bergkamp, J. J.; Sellinger, A.; Gust, D.; Rumbles, G. Local Intermolecular Order Controls Photoinduced Charge Separation at Donor/Acceptor Interfaces in Organic Semiconductors. *Adv. Energy Mater.* **2016**, *6* (6), 1–9.

(86) Provencher, F.; Bérubé, N.; Parker, A. W.; Greetham, G. M.; Towrie, M.; Hellmann, C.; Côté, M.; Stingelin, N.; Silva, C.; Hayes, S. C. Direct Observation of Ultrafast Long-Range Charge Separation at Polymer-Fullerene Heterojunctions. *Nat. Commun.* **2014**, *5*.

(87) Turner, S. T.; Pingel, P.; Steyrleuthner, R.; Crossland, E. J. W.; Ludwigs, S.; Neher, D. Quantitative Analysis of Bulk Heterojunction Films Using Linear Absorption Spectroscopy and Solar Cell Performance. *Adv. Funct. Mater.* **2011**, *21* (24), 4640–4652.

(88) Gann, E.; Young, A. T.; Collins, B. A.; Yan, H.; Nasiatka, J.; Padmore, H. A.; Ade, H.; Hexemer, A.;

Wang, C. Soft X-Ray Scattering Facility at the Advanced Light Source with Real-Time Data Processing and Analysis. *Rev. Sci. Instrum.* **2012**, *83* (4).

(89) Collins, B. A.; Cochran, J. E.; Yan, H.; Gann, E.; Hub, C.; Fink, R.; Wang, C.; Schuettfort, T.; McNeill, C. R.; Chabinyc, M. L.; et al. Polarized X-Ray Scattering Reveals Non-Crystalline Orientational Ordering in Organic Films. *Nat. Mater.* **2012**, *11* (6), 536–543.

(90) Hexemer, A.; Bras, W.; Glossinger, J.; Schaible, E.; Gann, E.; Kirian, R.; MacDowell, A.; Church, M.; Rude, B.; Padmore, H. A SAXS/WAXS/GISAXS Beamline with Multilayer Monochromator. *J. Phys. Conf. Ser.* **2010**, *247*, 0–11.

(91) Ilavsky, J. Nika: Software for Two-Dimensional Data Reduction. *J. Appl. Crystallogr.* **2012**, *45* (2), 324–328.

(92) Ferron, T.; Collins, B. A. RSoXS Data Reduction https://labs.wsu.edu/carbon/xray-analysis-tools/ (accessed Jan 1, 2018).